● *Original Contribution*

QUANTITATIVE ULTRASOUND AND B-MODE IMAGE TEXTURE FEATURES CORRELATE WITH COLLAGEN AND MYELIN CONTENT IN HUMAN ULNAR NERVE FASCICLES

Michal Byra,[*,†,§] Lidi Wan,[*,†] Jonathan H. Wong,[*,†] Jiang Du,[*,†] Sameer B. Shah,[*,‡]
Michael P Andre,[*,†] and Eric Y Chang[*,†]

* Research Service, VA San Diego Healthcare System, San Diego, California, USA; † Department of Radiology, University of
California, San Diego, California, USA; ‡ Departments of Orthopedic Surgery and Bioengineering, University of California,
San Diego, California, USA; and § Department of Ultrasound, Institute of Fundamental Technological Research, Polish Academy of
Sciences, Warsaw, Poland

Abstract—We investigate the usefulness of quantitative ultrasound and B-mode texture features for characterization of ulnar nerve fascicles. Ultrasound data were acquired from cadaveric specimens using a nominal 30-MHz probe. Next, the nerves were extracted to prepare histology sections. Eighty-five fascicles were matched between the B-mode images and the histology sections. For each fascicle image, we selected an intra-fascicular region of interest. We used histology sections to determine features related to the concentration of collagen and myelin and ultrasound data to calculate the backscatter coefficient (-24.89 ± 8.31 dB), attenuation coefficient (0.92 ± 0.04 db/cm-MHz), Nakagami parameter (1.01 ± 0.18) and entropy (6.92 ± 0.83), as well as B-mode texture features obtained *via* the gray-level co-occurrence matrix algorithm. Significant Spearman rank correlations between the combined collagen and myelin concentrations were obtained for the backscatter coefficient ($R = -0.68$), entropy ($R = -0.51$) and several texture features. Our study indicates that quantitative ultrasound may potentially provide information on structural components of nerve fascicles. (E-mail: mbyra@ucsd. edu)   © 2019 World Federation for Ultrasound in Medicine & Biology. All rights reserved.

Key Words: **Nerve, Quantitative ultrasound, High frequency, Histology, Pattern recognition, Texture analysis.**

INTRODUCTION

Ultrasound (US) is considered a first-line imaging modality for the clinical evaluation of peripheral nerves (Hayes et al. 2015; Rubin et al. 2018). However, important challenges that remain when imaging nerves with clinical scanners include limitations in resolution and reliance on subjective analyses. These limitations are exacerbated by the composite nature of nerve tissue, which comprises well-organized bundles of nerve fibers within a fascicle and bundles of fascicles within a whole nerve. Commonly utilized clinical US transducers for nerve imaging operate with maximal frequencies ranging from 15 to 22 MHz, with corresponding reported characteristic resolutions of approximately 0.1−0.2 mm (Moran et al. 2011).

To date, nerve characterization is most typically performed using B-mode US images, mainly to subjectively assess morphologic features of the whole nerve (Kane et al. 2004). B-Mode images have been used to detect and evaluate various pathologies of the peripheral nerves; for example. US can detect complete and partial nerve transections (Lawande et al. 2014). In the setting of carpal tunnel syndrome, nerves exhibit characteristic morphologic features in US images (Cartwright et al. 2012; Chan et al. 2011). Ultrasound systems with higher frequencies ranging from 20 to 100 MHz have been introduced into practice, mostly for eye and skin imaging (Lockwood et al. 1996). The first US scanners operating at frequencies up to 50 MHz were recently cleared by regulatory agencies for human use. These systems permit greater than threefold improvements in resolution and provide new ways to assess peripheral nerves. These high-frequency scanners can be used to provide clear delineation of nerve fascicle boundaries at certain locations, such as the median nerve at the wrist (Cartwright et al. 2017).

Quantitative ultrasound (QUS) is emerging as an exciting method to potentially reduce reliance on

subjective evaluation. Quantification can be employed on routine B-mode images to distinguish between normal and diseased nerves, such as through usage of the density function (fraction of the hypo-echoic pixels in a nerve) (Bignotti et al. 2015; Tagliafico et al. 2010), or can be used to improve nerve detection, such as through use of Gabor descriptors (Hadjerci et al. 2014). By use of raw radiofrequency (RF) US data, more fundamental ultrasonic parameters can now be quantified in a scanner-independent way, including the backscatter coefficient (BSC), attenuation coefficient (AC) and stochastic modeling of envelope statistics of backscattered echoes (Mamou and Oelze 2013). The BSC is a measure of a tissue's ability to backscatter US waves, providing information that is analogous, but not equal, to qualitative tissue echogenicity dependent on tissue structure and composition. The AC is related to the loss of energy that occurs in tissue during the wave propagation caused by absorption and scattering. Modeling of the backscatter echo statistics provides information about the spatial distribution of scattering microstructures within the resolution cell of the imaging transducer.

Quantitative US is now considered an efficient and reliable method of tissue characterization (Oelze and Mamou 2016) with wide-ranging applications including liver disease assessment (Lin et al. 2015; Zhou et al. 2018), breast mass characterization (Byra et al. 2016; Sadeghi-Naini et al. 2017) and evaluation of muscular changes (Weng et al. 2017). QUS methods have also been used with high-frequency data for characterization of the annular pulleys of the fingers (Lin et al. 2017b) and skin tissue (Pereyra and Batatia 2012; Piotrzkowska-Wroblewska et al. 2015). However, to the best of our knowledge, QUS methodology based on raw RF US data has not been applied to characterize human nerves or their fascicles using high frequencies. A non-invasive method that may potentially provide information on the structural components within nerve fascicles could have wide-reaching diagnostic and research applications. Therefore, the purpose of this study was to use US-based features, obtained from a clinical scanner capable of operating at ultrahigh frequencies (>20 MHz), for characterization of human ulnar nerve fascicles with histologic correlation. Specifically, we employed QUS features calculated from raw RF data, including the BSC, AC, Nakagami parameter and entropy, as well as texture features obtained *via* the gray-level co-occurrence matrix (GLCM) algorithm applied to B-mode images.

METHODS

Sample preparation

This prospective study was approved by our institutional review board with a waiver of informed consent for cadaveric specimen work. Six fresh-frozen cadaveric upper extremities with intact shoulder joints (three females, three males; mean age: 48.8 y; range: 21−70 y) were obtained from a non-profit whole-body donation company (United Tissue Network, Phoenix, AZ, USA) and included in this study. The specimens were disarticulated at the scapulothoracic and sternoclavicular articulations proximally and cut with a bandsaw at the mid-forearm distally. Specimens were stored in an ultra-low freezer ($-80°$C) and thawed in a room-temperature water bath for 24 h before scanning. Specimens underwent a single freeze−thaw cycle in total.

Data acquisition

Scanning was performed by a fellowship-trained musculoskeletal radiologist (8 y of experience with musculoskeletal US and radiologic−pathologic imaging correlation) using a clinical ultrahigh-frequency US scanner (Vevo MD, FUJIFILM, Toronto, ON, Canada), a linear probe with nominal 30-MHz center frequency (UHF48 transducer) and standard coupling gel. The sampling frequency was equal to 240 MHz The raw beamformed RF data were acquired using a constant time gain compensation, and the US signals were amplified with the same factor, which is independent of depth. Imaging was performed with the elbow in approximately 45° flexion and each ulnar nerve was scanned at nine distinct locations, 5 mm apart, centered at the level of the medial epicondyle, (Fig. 1a). Identical scanner settings were used during the data acquisition at each point. After each nerve was scanned, US raw data were acquired from a custom reference phantom (E. Madsen, University of Wisconsin, Madison, WI, USA), with homogeneous acoustic properties calibrated *a priori* over the range of frequencies encountered in this study. This additional phantom data acquisition was necessary for calculation of the QUS parameters (Yao et al. 1990) to normalize scanner-dependent conditions (beam focus, field of view, frequency, gain, *etc.*).

Histologic preparation

After US scanning, the specimens were carefully dissected (Fig. 1b). The roof of the cubital tunnel was released, and the epineurium of each ulnar nerve was labeled with a permanent marker while still *in situ* to facilitate accurate matching between the locations of the US image and the histology sections. The ulnar nerves were removed, fixed in 10% zinc formalin (Z-fix, Anatech LTD, Battle Creek, MI, USA), treated with 30% sucrose for cryoprotection and cut into 6-μm-thick cross sections. Staining with Masson's trichrome (Richard-Allen Scientific, Kalamazoo, MI, USA) was performed with incubation times of 10 min for Weigert's hematoxylin, 3 min for Biebrich scarlett−acid fuschin, 5 min for phosphotungstic acid and phosphomolybdic acid and
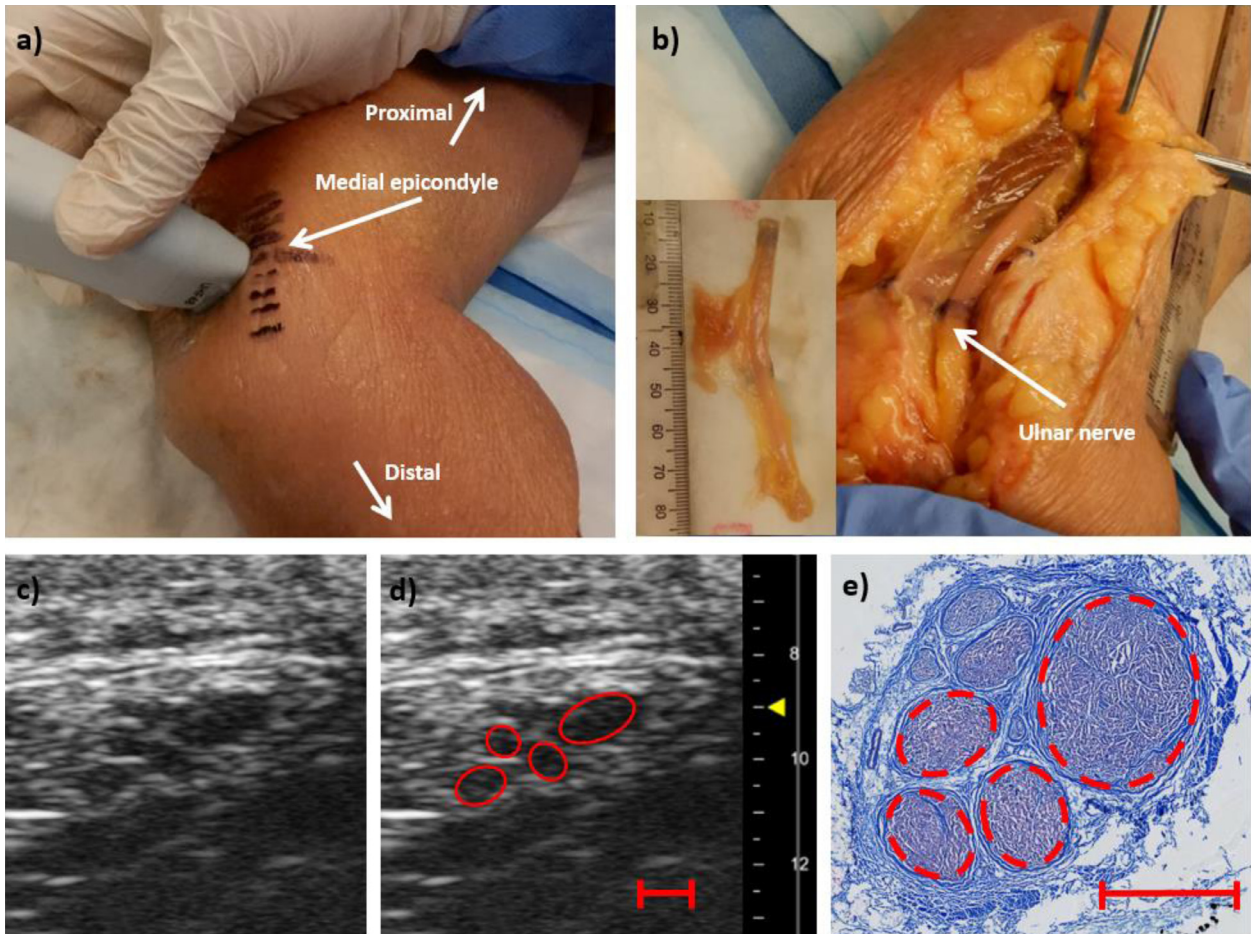
Fig. 1. (a) Each ulnar nerve was scanned at nine distinct locations, centered at the level of the medial epicondyle. (b) After the scanning, the cubital tunnel was released and nerve was removed. (c−e) The same fascicles on the B-mode image, (c) unlabeled and (d) labeled, and the (e) histology image were selected. Bar in millimeters.

5 min for aniline blue, to identify connective tissue (blue component) and myelinated axons (violet-red), which had a color distinct from the bright red of non-basophilic structures typically associated with trichrome staining.

Data analysis

Fifty-four pairs of histology and B-mode images were acquired (6 specimens, each with 9 spatially distinct imaging locations). The same musculoskeletal radiologist who performed the US scanning reviewed the pairs of images, matched the fascicles on the histology images to those on the B-mode images (Fig. 1c−e) and outlined the regions of interest (ROIs) indicating the fascicles. With respect to Figure 1, we note that the selected B-mode image is a single representative still image. The experienced radiologist had the benefit of real-time scanning, and at multiple locations in this specimen, and annotated images immediately after scanning to guide future analysis. Previous authors have similarly found that real-time scanning leads to improved structural

assessment (Clair et al. 1982; Van Holsbeke et al. 2008). Fascicles that were >1 mm in diameter were first identified on both the US and histology images. Based on these larger fascicles, histology images were either flipped or rotated to match the US images. Thereafter, attempts were made for inter-modality fascicle correlation based on size, spatial relationship and orientation relative to these larger fascicles. Only fascicles that could be well delineated for at least 50% of its perimeter were included. Specifically, fascicles were not included when the majority of the interface at the internal epineurial boundary was poor on the US images or the fascicles could not be confidently matched between modalities by an experienced musculoskeletal radiologist. An US medical physicist agreed upon the selected ROIs and confirmed the correspondence of fascicles. Moreover, matched fascicles were excluded from analysis when histology images contained obvious processing or sectioning artifacts, such as folds and tissue damage/separation. In total, 85 fascicles from 29 image pairs were included.
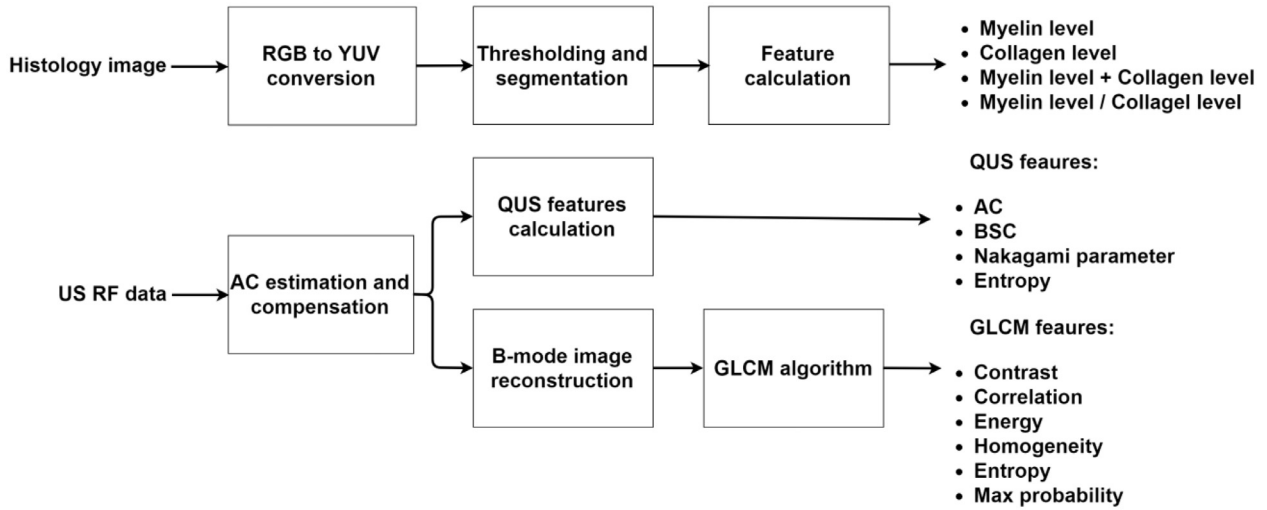
Fig. 2. Flowcharts illustrate histology and ultrasound feature extraction from nerve fascicles. The RGB histology images were transformed to YUV color space and color thresholded to extract pixels corresponding to ML and collagen. Raw ultrasound RF data were used to calculate quantitative parameters, and in the next step employed to reconstruct B-mode images and estimate GLCM features. AT = attenuation coefficient; GLCM = gray level co-occurrence matrix; RF = radio-frequency; QUS = quantitative ultrasound.

From the six specimens we extracted 3, 9, 11, 14, 20 and 28 pairs for the analysis, respectively.

Histology images were segmented using a color thresholding method (Fig. 2). First, the original red−green−blue (RGB) images were used to extract the white spaces. Second, each image was transformed from the RGB to the luminance−bandwidth−chrominance (YUV) color space to more easily separate the blue from the purple areas, indicating collagen (CL) and myelin (ML), respectively (Huisman et al. 2015; Turedi et al. 2018). In the case of the V chrominance component of the YUV color space, blue corresponds to the part of the color spectrum opposite to purple. After segmentation, the area fractions of regions positive for CL and ML were calculated. In addition, the ML-to-CL ratio and ML and CL sum (MCL) were calculated. All calculations were performed in MATLAB (Version 2018 a, The MathWorks, Natick, MA, USA).

Quantitative ultrasound features

Attenuation coefficient. Because of the tissue attenuation, US wave amplitude decreases with the propagation distance. The frequency-dependent attenuation is usually modeled using the equation

$$A(z) = A(z_0) - \alpha f z, \tag{1}$$

where $A(z)$ is the echo amplitude (in dB) decreased from the initial amplitude $A(z_0)$ at point z_0 over the propagation distance z, f is frequency and α (in dB/cm-MHz) is the AC. The AC can be estimated using the reference phantom with the formula

$$AC(f) = AC_{\text{phantom}}(f) - \frac{\gamma(f)}{4 * 8.686}, \tag{2}$$

where $AC_{\text{phantom}}(f)$ is the pre-computed reference phantom AC, and $\gamma(f)$ is the slope of the straight line that fits the log spectrum difference of the backscattered echoes in the tissue of interest and the reference phantom as a function of depth (Han et al. 2017).

Backscatter coefficient. The BSC quantifies the ability of the tissue to backscatter US energy and provides a measure of tissue "echogenicity." Similar to the AC, the BSC depends on the frequency of the imaging pulse, because the backscattering occurs on tissue microstructures that are small in comparison to the wavelength (Mamou and Oelze 2013). The BSC can be calculated using the reference phantom method after attenuation compensation using the equation (Han et al. 2017)

$$BSC(f) = \frac{S(f)}{S_{\text{phantom}}(f)} BSC_{\text{phantom}}(f) 10^{0.2(AC(f) - AC_{\text{phantom}}(f))} \tag{3}$$

where $S(f)$ and $S_{\text{phantom}}(f)$ are the sample and the reference phantom power spectrum functions, respectively. $BSC_{\text{phantom}}(f)$ is the pre-computed BSC for the reference phantom; the exponential factor is present in the equation because of the attenuation correction (Yao et al. 1990). The effects of beamforming and gain are compensated using the reference phantom method.

Envelope statistics. The Nakagami distribution was used to assess the envelope statistics of backscattered echoes in each nerve fascicle. The probability density function of the Nakagami distribution can be expressed as (Mohana Shankar 2000)

$$f_N(A) = \frac{2m^m A^{2m-1}}{\Gamma(m)\Omega^m} \exp\left(-\frac{m}{\Omega}A^2\right) \tag{4}$$

where A represents the backscattered echo amplitude, $\Gamma(\cdot)$ is the Gamma function and m and Ω are the shape and scaling parameters of the Nakagami distribution, respectively. The Nakagami parameter m is sensitive to the spatial distribution of tissue microstructures within the resolution cell of the imaging transducer. For $0.5 < m < 1$, the Nakagami distribution is pre-Rayleigh, interpreted as meaning the resolution cell contains a small number of strong scatterers mixed with the randomly distributed scatterers. For $m = 1$, the Nakagami distribution is identical to the Rayleigh distribution, and the resolution cell is expected to contain a large number of randomly distributed scatterers. For $m > 1$, the Nakagami distribution becomes Rician; the resolution cell contains a large number of randomly distributed scatterers along with regularly spaced scatters.

Additionally, the Shannon entropy of the backscattered echo amplitude was used for nerve characterization (Zimmer et al. 1996). In comparison to the Nakagami imaging, this is a different, model-free, approach to analysis of the backscattered echo statistics and has recently been applied for liver fat assessment (Tsui and Wan 2016; Zhou et al. 2018). The Shannon continuous entropy can be expressed as

$$\text{Entropy} = -\int_0^\infty f(A)\ln(f(A))\, dA, \tag{5}$$

where A is the US backscattered echo amplitude, and $f(A)$ refers to the probability density function of A. Entropy is also strictly related to the Nakagami distribution, for which entropy can be expressed as (Zimmer et al. 1996)

$$\text{Entropy}_{\text{Nakagami}} = \frac{1}{2}\ln \Omega + h(m), \tag{6}$$

where Ω and m are the parameters of the Nakagami distribution, and $h(m)$ is a function of the Nakagami parameter. Equation (5) clearly depicts that entropy is sensitive to the scaling of echo amplitudes (*e.g.*, because of the time-gain compensation) and requires attenuation correction, similar to the BSC, to be quantitative. After attenuation correction, it provides a parameter that jointly describes tissue echogenicity and backscattered envelope statistics.

Image texture analysis

Image texture analysis. Image texture analysis was performed using the GLCM algorithm (Haralick et al. 1973), a frequently employed technique in US imaging (Andrade et al. 2012; Bharti et al. 2017; Flores et al. 2015; Gaitini et al. 2004; Sadeghi-Naini et al. 2017). GLCM contains co-occurrence probabilities of all pairwise combinations of gray levels in an image or image region. Given a GLCM, the following six texture features were extracted: contrast, correlation, entropy, homogeneity, energy, maximum probability (Clausi 2002). These features quantify the fundamental properties of image texture related to its uniformity or how the pixels in the image are correlated with each other.

US feature calculation

The feature estimation flowchart is depicted in Figure 2. First, the frequency range of the backscattered echoes from the fascicles was determined using the Fourier transform as knowledge of the range of frequencies is important for QUS parameter calculation. The average center frequency of the backscattered echoes was determined to be approximately 16 MHz. The downshifted center frequency was expected for these high frequencies, caused by the attenuation of the US wave in the tissue layers superficial to the nerve (Klimonda et al. 2016). The BSC and AC were estimated for the frequency range as follows. Erosion operation was applied to clip each fascicle ROI and remove possible edge effects on the US parameter estimation. The ROIs were eroded with a circular window of size $\lambda/2$, where λ is the wavelength in water at 16 MHz. In the next step, each processed ROI was used to fit a square ROI. Square ROIs were used to keep the same number of samples in the RF signal lines oriented with the US A-lines. Next, to compensate attenuation effects in the nerve, the following strategy was employed. First, a uniform region of the tissue superficial to the nerve was selected and used to calculate the AC with the reference phantom method. Second, the AC in each fascicle using the square ROI and the reference phantom method was calculated. Next, both ACs were used to compensate for the effect of the attenuation in each fascicle ROI. The $\gamma(f)$ in eqn (2) was determined using the tissue and reference spectrum difference calculated for the frequency range $14-18$ MHz (central portion of the backscattered spectrum). Given $\gamma(f)$ and the reference phantom AC,

Table 1. Average values of the quantitative ultrasound parameters estimated for the data acquired from 85 fascicles

Parameter	AC (dB/cm-MHz)	BSC (dB)	Nakagami parameter	Entropy
Mean ± SD	0.92 ± 0.04	−24.89 ± 8.31	1.01 ± 0.18	6.92 ± 0.83
CV (SD/mean)	0.044	0.33	0.18	0.11

AC = attenuation coefficient; BSC = backscatter coefficient; CV = coefficient of variation; SD = standard deviation.

eqn (2) can be used to compute the fascicle ACs for the frequency range 14−18 MHz, and the averaged AC values over the range 15−17 MHz were used as the estimate of the AC for each fascicle (Han et al. 2017). After attenuation compensation, the BSC was estimated using the reference phantom method. As in the case of the AC, the BSC was calculated for frequencies between 14 and 18 MHz. Next, to obtain a single estimate, the BSC was averaged over the range 15−17 MHz. To calculate the envelope statistics parameters, the Hilbert transform was applied to compute RF signal amplitude, and the amplitude samples were extracted using the eroded fascicle ROI. The Nakagami parameter was calculated using the maximum likelihood estimator (Lin et al. 2017a). Entropy was calculated using eqn (5).

There are two parameters associated with the GLCM algorithm: the distance path (inter-pixel distance) and the orientation angle. In the case of US B-mode images, the distance path was set to be equal to $\lambda/4$ and the orientation angle was set to 90°. Only the co-occurrence of the gray-level values in the axial direction were analyzed.

Statistics

Descriptive statistics were calculated, including mean, standard deviation (SD) and coefficient of variation (CV). Correlations between US and histology features, as well as between various US features, were performed using Spearman's rank. In addition, because adjustment of threshold levels of the B-mode images is commonly used in clinical practice to enhance contrast, effects of B-mode image reconstruction on the performance of the GLCM-based features were also evaluated. The B-mode images were reconstructed from the amplitude samples, which were logarithmically compressed using the equation

$$A_{\log} = 20\log_{10}\left(\frac{A}{A_{\max}}\right) \tag{7}$$

where A and $A_{\log}$ are the amplitude and the logarithmically compressed amplitude of the ultrasonic RF signal, respectively. $A_{\max}$ indicates the highest value of the amplitude found in the RF data. For a specific threshold level, the log-compressed amplitude was mapped to the range [0, 255] (8 bits). B-Mode images were reconstructed using threshold levels of [30, 35, 40, 45, 50, 55, 60] dB, which are commonly employed in US imaging.

Next, we investigated the impact of the reconstruction threshold level on the correlation between B-mode based features and histology findings.

RESULTS

The average fascicle area, measured using histology images, was equal to 0.81 ± 0.59 mm. The estimated QUS parameters for the data acquired from all nerve fascicles are summarized in Table 1. The smallest CV value was obtained for the AC (CV = 0.044), suggesting that the fascicles attenuated the US waves comparably. The highest CV value was obtained for the BSC (CV = 0.33). The high dynamic range of the BSC (CV almost 10 times more than the AC) suggests high variability in the biological/structural contribution to this measure.

The Spearman rank correlation results between US and histology features are outlined in Table 2. Changes in US parameters were related mainly to the variation of CL in the fascicles. The highest correlation coefficient ($\rho = -0.68$) was obtained for the BSC and the MCL. Negative correlation coefficients indicate that the BSC decreases with MCL (Fig. 3). Entropy had a lower, but still statistically significant coefficient ($\rho = -0.51$). Statistically significant correlation coefficients were not obtained for the Nakagami parameter or the AC. There was also no significant correlation between the fascicular areas determined in histology and the features related to CL and ML concentrations.

The Spearman rank correlation results between various US features are depicted in Table 3 and Figure 4,

Table 2. Spearman's rank correlation coefficients between the ultrasound features and the histology findings

Parameter	ML/CL	ML	CL	MCL
Attenuation coefficient	0.01	−0.05	−0.06	−0.05
Backscatter coefficient	0.01	−0.20	−0.56*	−0.68*
Nakagami parameter	−0.08	−0.11	−0.021	−0.09
Entropy	0.09	−0.07	−0.47*	−0.51*
GLCM contrast	0.11	−0.08	−0.58*	−0.63*
GLCM correlation	−0.09	−0.02	0.16	0.15
GLCM energy	−0.09	0.09	0.55*	0.59*
GLCM homogeneity	−0.09	0.01	0.59*	0.64*
GLCM entropy	0.10	−0.07	−0.52*	−0.55*
GLCM max prob	−0.05	0.13	0.56*	0.62*

CL = collagen; GLCM = gray-level co-occurrence matrix; MCL = sum of CL and ML; ML = myelin.
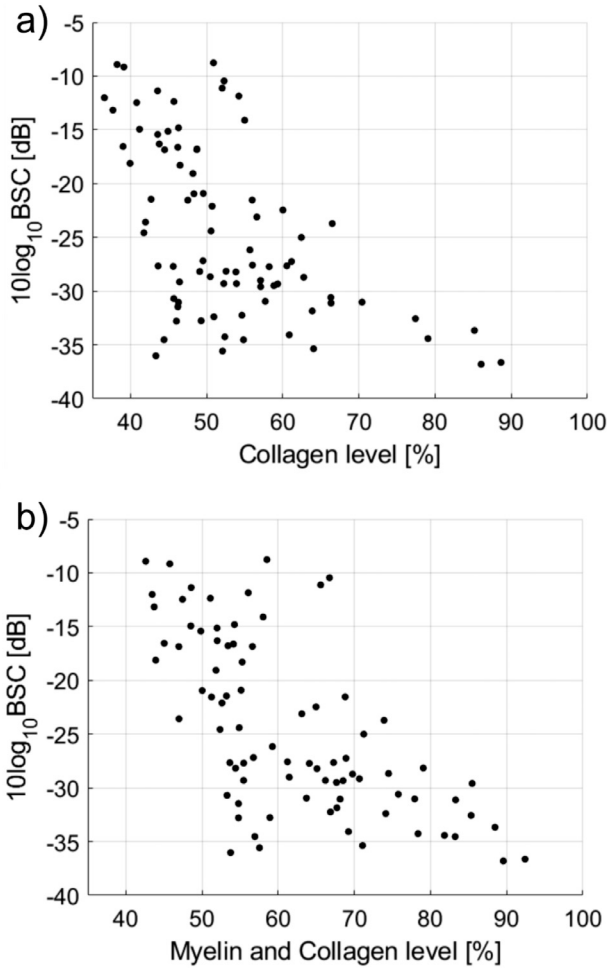* Statistically significant ($p < 0.001$).

Fig. 3. (a) Relationship between backscatter coefficient (BSC) and collagen level: correlation coefficient = −0.56. (b) Relationship between BSC and sum of myelin and collagen levels: correlation coefficient = −0.68.

which indicate that the GLCM-based features are overall highly correlated with each other. Additionally, entropy and the BSC are correlated, which is expected because both assess tissue echogenicity. Additionally, high correlation coefficients between BSC, entropy and the
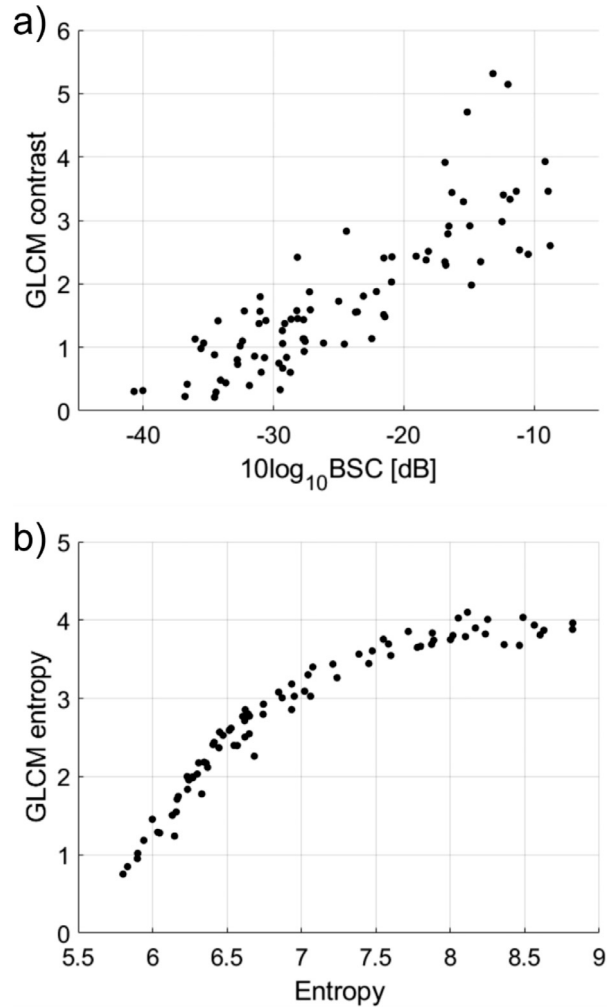

Fig. 4. Relationship between quantitative ultrasound parameters and gray level co-occurrence matrix (GLCM)-based features. (a) For the backscatter coefficient (BSC) the highest correlation coefficient was obtained for the GLCM contrast: 0.87. (b) Relationship between quantitative ultrasound entropy and GLCM entropy: correlation coefficient = 0.98.

GLCM-based features were obtained. As would be expected, QUS entropy was highly correlated with GLCM entropy, and a high value for the BSC

Table 3. Spearman's rank correlation matrix for the ultrasound features

Parameter	AC	BSC	Nakagami	Entropy	GLCM$_{contrast}$	GLCM$_{correlation}$	GLCM$_{energy}$	GLCM$_{homogeneity}$	GLCM$_{entropy}$	GLCM$_{maxprob}$
AC	1									
BSC	0.21	1								
Nakagami	−0.37	−0.09	1							
Entropy	0.39	0.82	−0.43	1						
GLCM$_{contrast}$	0.34	0.87	−0.28	0.94	1					
GLCM$_{correlation}$	0.34	0.12	−0.65	0.44	0.17	1				
GLCM$_{energy}$	−0.41	−0.83	0.32	−0.95	−0.95	−0.31	1			
GLCM$_{homogeneity}$	−0.36	−0.85	0.25	−0.92	−0.99	−0.17	0.97	1		
GLCM$_{entropy}$	0.40	0.84	−0.38	0.98	0.96	0.36	−0.99	−0.96	1	
GLCM$_{maxprob}$	−0.40	−0.83	−0.26	−0.92	−0.94	−0.28	0.98	0.96	−0.97	1

AC = attenuation coefficient; BSC = backscatter coefficient; GLCM = gray level co−occurrence matrix, respectively.
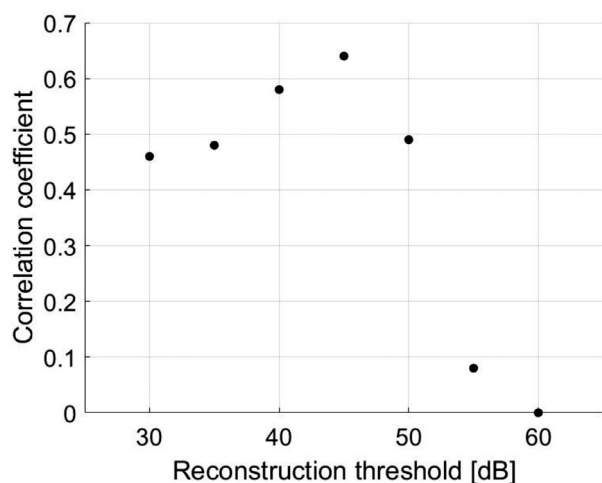
Fig. 5. Impact of B-mode image reconstruction threshold level on correlation coefficient between gray-level co-occurrence matrix homogeneity and sum of myelin and collagen levels. Based on this plot, the 45-dB reconstruction threshold was used for subsequent analysis.

corresponded to a high value for B-mode image texture homogeneity.

Evaluation of the B-mode image reconstruction threshold level on performance of GLCM-based features revealed that the best performance was obtained for a threshold level of around 45 dB. Figure 5 illustrates how Spearman's correlation coefficient between the homogeneity feature and the MCL is modified by the modification of the threshold level. For high threshold values, the image was dominated by noise, and the GLCM feature correlated poorly with histology. Similarly, small threshold values resulted in lower performance because of compression of speckle patterns that corresponded to lower-amplitude echoes. These small amplitude values lost their image conspicuity. For analysis used in the remainder of the study, GLCM-based features were calculated using the threshold level of 45 dB. As in the case of the QUS parameters, the GLCM-based features were related to CL and MCL (Table 2). The highest correlation coefficient was obtained for the homogeneity feature, which measures the uniformity of image texture, and MCL ($\rho = 0.64$) (Fig. 6).

DISCUSSION

In our study, we used US-based features for ulnar nerve characterization. We imaged the nerve *in situ* at room temperature within the cubital tunnel of cadaveric elbow specimens and successfully matched a large number of the fascicles on the B-mode and histology images. For the matched fascicles, several QUS parameters correlated with histologic outcomes, with the highest correlation coefficient of −0.68 for BSC versus MCL.
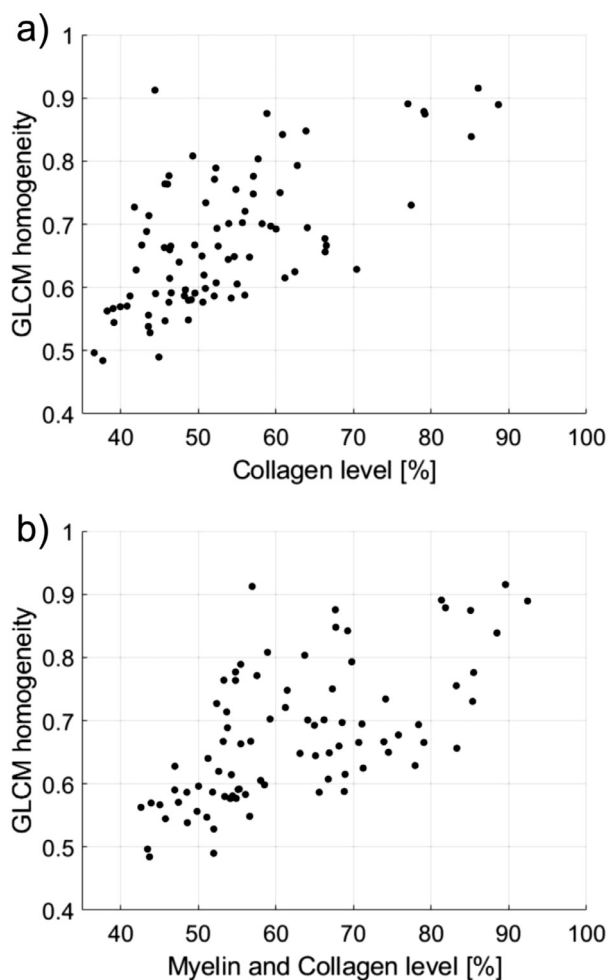

Fig. 6. (a) Relationship between gray-level co-occurrence matrix (GLCM) homogeneity and collagen level: correlation coefficient = 0.59. (b) Relationship between GLCM homogeneity and the sum of myelin and collagen levels: correlation coefficient = 0.64.

Table 2 illustrates that the US parameters were mostly related to the CL variations calculated using the segmented histology images. A negative correlation coefficient between BSC and CL suggests that high connective tissue concentration in the fascicles results in a low value of the BSC or lower overall tissue echogenicity. Backscattering of US waves occurs at interfaces of tissue microstructures that have different physical properties (*e.g.,* sound speed, density) (Mamou and Oelze 2013). In a material that has uniform spatial distribution of the physical properties (*e.g.,* local density), the scattering would be low. Our results may agree with this observation; as CL decreases, fascicle composition tends to be less uniform, with a possibly larger number of different tissue interfaces that contribute to the backscattering. Moreover, the correlation coefficient between BSC and MCL was higher than that between BSC and CL,

which suggests that the ML concentration also has an impact on backscattering. The AC did not correlate with the histology findings. The average value of the AC was 0.92 dB/cm-MHz, higher than the average value of AC in human soft tissue, 0.54 dB/cm-MHz, or the brain, 0.6 dB/cm-MHz (Culjat et al. 2010; Mast 2000) and highly invariable across fascicles (low CV). The Nakagami parameter also did not correlate well with the histology findings. This may be explained by the average Nakagami parameter of the fascicles, which was close to 1 (Rayleigh scattering), indicating that the investigated tissue contains a large number of randomly distributed scatterers. The Nakagami parameter mostly provides information about the relative scattering scenario occurring in a particular tissue rather than a quantitative assessment of tissue microstructure.

The correlation coefficients obtained for the GLCM-based features were slightly lower than those for the BSC, with the highest coefficient equal to 0.64 for the GCLM homogeneity feature. The GLCM features, however, were highly correlated with the BSC and entropy, suggesting that these features, as expected, are related to the backscattering properties of the tissue. The estimation of GLCM features is more scanner dependent than that of QUS features. Our results regarding modification of the threshold levels clearly illustrate this issue (Fig. 5). For researchers interested in tissue characterization, QUS parameters would be recommended as the preferential first-line tool. However, if RF data acquisition is not possible, because of the limitations of the scanner, the GLCM-based approaches should also be useful. In this scenario, investigators should be aware of the pitfalls and limitations of B-mode image texture analysis and attempt to maintain identical scanner settings and tissue geometry during measurements to compensate for the effects of attenuation.

Several studies have previously reported a relationship between tissue echogenicity and CL concentration, for native tissues such as the intestines (Kimmey et al. 1989) and engineered tissues (Deng et al. 2016; Mercado et al. 2015). To the best of our knowledge, ours is the first study to utilize QUS methods to assess the physical properties of nerve fascicles. The correlation between US features and fascicle CL and ML content determined in our study may be useful for the non-invasive assessment of peripheral nerve composition and changes. Importantly, our results indicate that this information may not be determined simply by measuring cross-sectional area. Similar to our results, one study found that morphologic determinations of cross-sectional area along the ulnar nerve did not correlate with quantitative CL data (McFarlane et al. 1980). Assessment of CL can be important as it varies widely depending on nerve location (McFarlane et al. 1980) and/or its physiologic

or biomechanical environment. For example, nerve immobilization results in ML degeneration and deposition of CL in the endoneurium (Culjat et al. 2010).

Our results complement those from several other investigators who have suggested that QUS can be used to characterize nerves. The AC parameter of the whole rat sciatic nerve *in vitro* was used to estimate nerve damage caused by diabetic peripheral neuropathy (Chen et al. 2014). Tissue echogenicity was assessed *via* the nerve density measure and was found to be an important factor in diagnosis of carpal tunnel syndrome (Tagliafico et al. 2010). In future work, we plan to compare B-mode measures with QUS measures to assess diagnostic performance. QUS methodology can also be used to monitor nerve regeneration (Schmidt and Leach 2003; Wood et al. 2011) and to measure temperature changes in nerve during high-intensity focus US treatment (Foley et al. 2008; Lewis et al. 2015).

There are several limitations to our study. First, the US data were acquired from cadaveric specimens that underwent a freeze−thaw cycle, likely affecting imaging outcomes and histologic quality. Caution should be exercised when comparing our results with *in vivo* data. Second, acquisition of the US data, the specimens were dissected to extract the ulnar nerve in preparation for histology. Although this was carefully performed, the histology images may not correspond exactly to the imaging plane of the US transducer or represent any distortion in geometry imposed by surrounding anatomic structures *in situ*. Third, outlining of the same fascicles on the B-mode and histology images was performed by an experienced radiologist, but for several B-mode images the visibility of the fascicles was too poor to delineate the fascicles with high confidence. Of note, an *in vivo* study utilizing a higher-frequency transducer (nominal center frequency = 50 MHz) on the median nerve at a superficial location noted similar findings where some fascicles were easier to depict than others (Cartwright et al. 2017). One explanation for this may be that the ulnar nerves were imaged with the elbows in approximately 45° flexion. At submaximal tension, especially in the highly compliant joint region of the ulnar nerve, there may be intra-neural fascicular undulations or bending (Shah 2017), resulting in an oblique imaging plane or potential volume averaging. Fourth, our modeling of the nerve fascicle was incomplete as evidenced by the inability for the variability of BSC, or any other US feature employed in our study, to be fully explained by variability in the connective tissue and ML content. Indeed, modeling of tissue is challenging because there are several factors that contribute to backscattering and speckle patterns. We did not investigate the effects of tissue microstructure orientation and position on backscattering (Han and O'Brien 2015), we did not evaluate CL microarchitecture in three dimensions and we used

information from only one histologic stain. It is possible that additional nerve constituents that may have been highlighted by different histologic preparations or immunostains may have further improved the correlations. Fifth, we limited our analysis to intra-fascicular regions, given the ambiguity of perineurial and epineurial boundaries in US images. Therefore, the role of extra-fascicular CL on QUS outcomes remains an interesting and important area of future work. Finally, though a medical physicist agreed upon ROI selection and confirmed fascicular correspondence between B-mode and histologic images, and though there is typically strong reproducibility in nerve morphology and echogenicity measurements among different operators (Cartwright et al. 2017; Tagliafico et al. 2010), our study included only one musculoskeletal radiologist for scanning and fascicle correlation. Therefore, we were unable to assess the reproducibility of US measurements for different operators, scanners or transducers. Future work will investigate these variables and also consider employing automatic fascicle segmentation algorithms.

In this work we investigated the usefulness of two US-based approaches for nerve characterization. The first one utilized QUS methods, and the second was related to B-mode texture analysis with the GLCM. Our study found that both approaches may be useful for nerve characterization, as both yielded significant correlations with histologic CL and MCL. However, the usefulness of the GLCM-based features depended on the B-mode image reconstruction algorithm applied. Our study suggests that QUS methods, which are scanner independent, should be favored. If access to raw US data is limited, the GLCM-based approach still can provide useful information about the investigated tissue.

Conflict of interest disclosure—The authors do not have any conflicts of interest.

REFERENCES

Andrade A, Silva JS, Santos J, Belo-Soares P. Classifier approaches for liver steatosis using ultrasound images. Proc Technol 2012;5:763–770.

Bharti P, Mittal D, Ananthasivan R. Computer-aided characterization and diagnosis of diffuse liver diseases based on ultrasound imaging: A review. Ultrason Imaging 2017;39:33–61.

Bignotti B, Ghio M, Panico N, Tagliafico G, Martinoli C, Tagliafico A. High-resolution ultrasound of peripheral nerves in systemic sclerosis: A pilot study of computer-aided quantitative assessment of nerve density. Skeletal Radiol 2015;44:1761–1767.

Byra M, Nowicki A, Wroblewska-Piotrzkowska H, Dobruch-Sobczak K. Classification of breast lesions using segmented quantitative ultrasound maps of homodyned K distribution parameters. Med Phys 2016;43:5561–5569.

Cartwright MS, Hobson-Webb LD, Boon AJ, Alter KE, Hunt CH, Flores VH, Werner RA, Shook SJ, Thomas TD, Primack SJ, Walker FO. Evidence-based guideline: Neuromuscular ultrasound for the diagnosis of carpal tunnel syndrome. Muscle Nerve 2012;46:287–293.

Cartwright MS, Baute V, Caress JB, Walker FO. Ultrahigh-frequency ultrasound of fascicles in the median nerve at the wrist. Muscle Nerve 2017;56:819–822.

Chan KY, George J, Goh KJ, Ahmad TS. Ultrasonography in the evaluation of carpal tunnel syndrome: Diagnostic criteria and comparison with nerve conduction studies. Neurology Asia 2011;16:57–64.

Chen GS, Lee YF, Cheng JS. Measurement of ultrasonic attenuation in diabetic neuropathic sciatic nerves for diagnostic and therapeutic applications. Ann Biomed Eng 2014;42:1749–1759.

Clair MR, Rosenberg ER, Ram PC, Bowie JD. Comparison of real−time and static-mode gray−scale ultrasonography in the diagnosis of cholelithiasis. J Ultrasound Med 1982;1:201–203.

Clausi DA. An analysis of co-occurrence texture statistics as a function of grey level quantization. Can J Remote Sensing 2002;28:45–62.

Culjat MO, Goldenberg D, Tewari P, Singh RS. A review of tissue substitutes for ultrasound imaging. Ultrasound Med Biol 2010;36:861–873.

Deng CX, Hong X, Stegemann JP. Ultrasound imaging techniques for spatiotemporal characterization of composition, microstructure, and mechanical properties in tissue engineering. Tissue Eng Part B Rev 2016;22:311–321.

Flores WG, Pereira WCA, Infantosi AFC. Improving classification performance of breast lesions on ultrasonography. Pattern Recogn 2015;48:1125–1136.

Foley JL, Little JW, Vaezy S. Effects of high-intensity focused ultrasound on nerve conduction. Muscle Nerve 2008;37:241–250.

Gaitini D, Baruch Y, Ghersin E, Veitsman E, Kerner H, Shalem B, Yaniv G, Sarfaty C, Azhari H. Feasibility study of ultrasonic fatty liver biopsy: Texture vs. attenuation and backscatter. Ultrasound Med Biol 2004;30:1321–1327.

Hadjerci O, Hafiane A, Makris P, Conte D, Vieyres P, Delbos A. Nerve detection in ultrasound images using median Gabor binary pattern. Cham: Springer International; 2014. p. 132–140.

Han A, O'Brien W, Jr. Structure function for high-concentration biophantoms of polydisperse scatterer sizes. IEEE Trans Ultrason Ferroelectr Freq Control 2015;62:303–318.

Han A, Andre MP, Erdman JW, Loomba R, Sirlin CB, O'Brien WD. Repeatability and reproducibility of a clinically based QUS phantom study and methodologies. IEEE Trans Ultrason Ferroelectr Freq Control 2017;64:218–231.

Haralick RM, Shanmugam K, Dinstein I. Textural features for image classification. IEEE Trans Syst Man Cybernet 1973;SMC-3:610–621.

Hayes CW, Roberts CC, Bencardino JT, Appel M, Arnold E, Baccei SJ, Chang EY, Fox MG, Fries IB, Greenspan BS, Hochman MG, Murphey MD, Newman JS, Rosenberg ZS, Rubin DA, Small K, Weissman BN. Expert Panel on Musculoskeletal Imaging. 2015 ACR Appropriateness Criteria® Chronic Elbow Pain. Reston, VA: American College of Radiology; 2015.

Huisman M, Staruch RM, Ladouceur-Wodzak M, van den Bosch MA, Burns DK, Chhabra A, Chopra R. Non-invasive targeted peripheral nerve ablation using 3-D MR neurography and MRI-guided high-intensity focused ultrasound (MR-HIFU): Pilot study in a swine model. PLoS One 2015;10 e0144742.

Kane D, Grassi W, Sturrock R, Balint PV. Musculoskeletal ultrasound—A state of the art review in rheumatology: Part 2. Clinical indications for musculoskeletal ultrasound in rheumatology. Rheumatology (Oxford) 2004;43:829–838.

Kimmey MB, Martin RW, Haggitt RC, Wang KY, Franklin DW, Silverstein FE. Histologic correlates of gastrointestinal ultrasound images. Gastroenterology 1989;96:433–441.

Klimonda Z, Postema M, Nowicki A, Litniewski J. Tissue attenuation estimation by mean frequency downshift and bandwidth limitation. IEEE Trans Ultrason Ferroelectr Freq Control 2016;63:1107–1115.

Lawande AD, Warrier SS, Joshi MS. Role of ultrasound in evaluation of peripheral nerves. Indian J Radiol Imaging 2014;24:254–258.

Lewis MA, Staruch RM, Chopra R. Thermometry and ablation monitoring with ultrasound. Int J Hyperthermia 2015;31:163–181.

Lin SC, Heba E, Wolfson T, Ang B, Gamst A, Han A, Erdman JW Jr, O'Brien WD Jr, Andre MP, Sirlin CB, Loomba R. Noninvasive diagnosis of nonalcoholic fatty liver disease and quantification of liver fat using a new quantitative ultrasound technique. Clin Gastroenterol Hepatol 2015;13:1337–1345 e6.

Lin JJ, Cheng JY, Huang LF, Lin YH, Wan YL, Tsui PH. Detecting changes in ultrasound backscattered statistics by using Nakagami parameters: Comparisons of moment-based and maximum likelihood estimators. Ultrasonics 2017a;77:133–143.

Lin YH, Yang TH, Wang SH, Su FC. Quantitative assessment of first annular pulley and adjacent tissues using high-frequency ultrasound. Sensors (Basel) 2017b;17:107.

Lockwood GR, Turnball DH, Christopher DA, Foster F. Beyond 30 MHz - Applications of high frequency ultrasound imaging. IEEE Eng Med Biol Mag 1996;15:60–71.

Mamou J, Oelze ML. Quantitative ultrasound in soft tissues. Dordrecht: Springer; 2013.

Mast TD. Empirical relationships between acoustic parameters in human soft tissues. Acoust Res Lett Online 2000;1:37–42.

McFarlane KR, Pollock M, Myers DB. Collagen content in human ulnar nerve. Acta Neuropathol 1980;50:217–220.

Mercado KP, Helguera M, Hocking DC, Dalecki D. Noninvasive quantitative imaging of collagen microstructure in three-dimensional hydrogels using high-frequency ultrasound. Tissue Eng Part C Methods 2015;21:671–682.

Mohana Shankar P. A general statistical model for ultrasonic backscattering from tissues. IEEE Trans Ultrason Ferroelectr Freq Control 2000;47:727–736.

Moran CM, Pye SD, Ellis W, Janeczko A, Morris KD, McNeilly AS, Fraser HM. A comparison of the imaging performance of high resolution ultrasound scanners for preclinical imaging. Ultrasound Med Biol 2011;37:493–501.

Oelze ML, Mamou J. Review of quantitative ultrasound: Envelope statistics and backscatter coefficient imaging and contributions to diagnostic ultrasound. IEEE Trans Ultrason Ferroelectr Freq Control 2016;63:336–351.

Pereyra M, Batatia H. Modeling ultrasound echoes in skin tissues using symmetric alpha-stable processes. IEEE Trans Ultrason Ferroelectr Freq Control 2012;59:60–72.

Piotrzkowska-Wroblewska H, Litniewski J, Szymanska E, Nowicki A. Quantitative sonography of basal cell carcinoma. Ultrasound Med Biol 2015;41:748–759.

Rubin DA, Roberts CC, Bencardino JT, Bell AM, Cassidy RC, Chang EY, Gyftopoulos S, Metter DF, Morrison WB, Subhas N, Tambar S, Towers JD, Yu JS, Kransdorf MJ. Expert Panel on Musculoskeletal Imaging. ACR Appropriateness Criteria® Chronic Wrist Pain. J Am Coll Radiol 2018;15:S39–S55.

Sadeghi-Naini A, Suraweera H, Tran WT, Hadizad F, Bruni G, Rastegar RF, Curpen B, Czarnota GJ. Breast-lesion characterization using textural features of quantitative ultrasound parametric maps. Sci Rep 2017;7:13638.

Schmidt CE, Leach JB. Neural tissue engineering: Strategies for repair and regeneration. Annu Rev Biomed Eng 2003;5:293–347.

Shah SB. Tissue biomechanics: Whales have some Nnerve. Curr Biol 2017;27:R177–R179.

Tagliafico A, Tagliafico G, Martinoli C. Nerve density: A new parameter to evaluate peripheral nerve pathology on ultrasound: Preliminary study. Ultrasound Med Biol 2010;36:1588–1593.

Tsui PH, Wan YL. Effects of fatty infiltration of the liver on the Shannon entropy of ultrasound backscattered signals. Entropy 2016;18:341.

Turedi S, Yulug E, Alver A, Bodur A, Ince I. A morphological and biochemical evaluation of the effects of quercetin on experimental sciatic nerve damage in rats. Exp Ther Med 2018;15:3215–3224.

Van Holsbeke C, Yazbek J, Holland TK, Daemen A, De Moor B, Testa AC, Valentin L, Jurkovic D, Timmerman D. Real−time ultrasound vs. evaluation of static images in the preoperative assessment of adnexal masses. Ultrasound Obstet Gynecol 2008;32:828–831.

Weng WC, Tsui PH, Lin CW, Lu CH, Lin CY, Shieh JY, Lu FL, Ee TW, Wu KW, Lee WT. Evaluation of muscular changes by ultrasound Nakagami imaging in Duchenne muscular dystrophy. Sci Rep 2017;7:4429.

Wood MD, Kemp SW, Weber C, Borschel GH, Gordon T. Outcome measures of peripheral nerve regeneration. Ann Anat 2011;193:321–333.

Yao LX, Zagzebski JA, Madsen EL. Backscatter coefficient measurements using a reference phantom to extract depth-dependent instrumentation factors. Ultrason Imaging 1990;12:58–70.

Zhou Z, Tai DI, Wan YL, Tseng JH, Lin YR, Wu S, Yang KC, Liao YY, Yeh CK, Tsui PH. Hepatic steatosis assessment with ultrasound small-window entropy imaging. Ultrasound Med Biol 2018;44:1327–1340.

Zimmer Y, Akselrod S, Tepper R. The distribution of the local entropy in ultrasound images. Ultrasound Med Biol 1996;22:431–439.